Determining the Momentum Width of a Trapped Bose-Einstein Condensate by One-Dimensional-Optical-Lattice Pulse Sequences

Angang Liang,[1,2,3] Shuyu Zhou,[3,*] Yu Xie,[1,2,3] Mingshan Huang,[1,2,3] Xinping Xu,[1] Su Fang,[1] Dijun Chen,[1] Tang Li,[1] Bin Wang,[1] Weibiao Chen,[1] and Liang Liu[1,†]

[1]*Space Laser Engineering Center, Shanghai Institute of Optics and Fine Mechanics, Chinese Academy of Sciences, Shanghai 201800, China*

[2]*Center of Materials Science and Optoelectronics Engineering, University of Chinese Academy of Sciences, Beijing 100049, China*

[3]*Key Laboratory for Quantum Optics, Shanghai Institute of Optics and Fine Mechanics, Chinese Academy of Sciences, Shanghai 201800, China*

We experimentally verified our prior theoretical work [J. Opt. Soc. Am. B **39**, 3012 (2022)] by employing matter-wave interference to measure the ultranarrow momentum width of an optically trapped Bose-Einstein condensate (BEC) *in situ*. Splitting the BEC wave packet into various diffraction orders through double stand-wave pulses, we calibrated the momentum width by fitting the oscillation curve of the population of the zero-momentum state. The observed interference fringes exhibited slight deviations from our simplified theory. We numerically calculated the *Gross-Pitaevskii* equation and utilized Wigner function to gain insight into the impact of the external trap potential and nonlinear term of BEC. We found that the discrepancy was caused by the combined effects of the mean-field interaction and spatial density modulation of BEC. This quantum thermometry is straightforward to apply and is especially well suited for temperature calibration in deep cooling experiments. For atomic samples at the pK level after deep cooling, interatomic interactions can be safely disregarded, enabling momentum-width calibration in a single shot.

I. INTRODUCTION

Over the past two decades, the research on quantum degenerate gases has witnessed substantial advancements, offering a distinctive platform for various pioneering discoveries and technological innovations [1,2]. The attainment of even lower temperatures of atomic ensembles would facilitate the examination of quantum mechanics at a more macroscopic level [3,4]. Currently, in addition to traditional evaporative cooling [5], the state-of-the-art δ-kick collimation [6,7] (DKC) technology has reduced the equivalent temperature of BEC to several tens of picokelvin [8,9]. Combining with microgravity environment, these quantum gases are expected to be used as analogues for more inaccessible quantum systems [10–14]. Additionally, the extremely long free-expansion time of these systems fulfills the stringent requirements of atomic interferometers, which can be applied to the most advanced quantum precision measurement [15–21].

However, the extremely low kinetic energy also poses a challenge for thermometry. Conventional time-of-flight (TOF) method [22] become inefficient and susceptible to spatial stray fields due to excessive flight time [8,9]. For measuring extremely low temperatures, those Raman [23] and Bragg Doppler spectroscopy [24,25] require strict control of the frequency and phase coherence of the laser beams, while the measurement-induced perturbations of the velocity distribution cannot be neglected.

The nonzero momentum width also implicates a finite spatial coherence length [26,27], which can be used to calibrate temperature [28–30]. In this paper, we validate our previous theoretical work on quantum thermometry based on atomic interference [31]. By utilizing appropriate Bragg pulse as $\pi/2$ pulse, Ramsey interference is performed on momentum states of a trapped BEC. Due to the finite coherence length, the contrast of the interference fringes decays with increasing Ramsey free-evolution time, therefore the one-dimensional momentum width (1D MW) of the BECs can be obtained *in situ*. Furthermore, a detailed analysis of the impact of the mean-field interaction of the confined BEC on the interference process is presented.

*syz@siom.ac.cn
†liang.liu@siom.ac.cn

II. DOUBLE 1D OPTICAL LATTICE PULSE-SPLITTING THERMOMETRY

Off-resonant standing-wave laser pulses are widely employed in atomic interference to split matter waves into various diffracted orders [32,33]. An appropriate double Bragg pulse sequence can symmetrically split the wave packet into $\pm 2\hbar k_0$ superposition states with nearly 100% efficiency, where k_0 represents the laser wave vector and $\hbar$ donates the reduced Planck constant. The interaction between matter wave packets and weak standing-wave fields can be described by the truncated Raman-Nath equations [34]. By introducing the coupled bases $|C_0(k)\rangle$, $|C_+(k)\rangle = (|C_{+2k_0}(k)\rangle + |C_{-2k_0}(k)\rangle)/\sqrt{2}$, $|C_-(k)\rangle = (|C_{+2k_0}(k)\rangle - |C_{-2k_0}(k)\rangle)/\sqrt{2}$, where $|C_{2nk_0}|^2$ represents the population of the nth diffraction order with momentum $\hbar k + 2n\hbar k_0$, a narrow distribution around $k = 0$ ($\Delta k \ll k_0$) can render $|C_-\rangle$ a dark state that can be disregarded, therefore the state space reduces into a two-state system that can be mapped to a unit Bloch sphere. The double-pulse-splitting operation is associated with the well-known Ramsey interferometer [35], which achieves a bit flip from the perspective of quantum logic gate. By choosing $\Omega = 2\sqrt{2}\omega_r$ during the pulse duration, where Ω describes the amplitude of the light-shift potential ($\omega_r = \hbar k_0^2/2m$ and m is the atomic mass), the standard Ramsey technique for reversing the state vector is illustrated in Fig. 1(a).

The nonzero momentum width of the packet will degrade the splitting efficiency as the free-evolution time increases, and further deteriorates the contrast of the interference signal [27]. For a matter wave packet with a momentum distribution of $|\Phi(k)|^2$, by fixing the pulse duration $t_1 = \pi/4\sqrt{2}\omega_r$ [corresponding to $n = 0$, see Fig. 1(a)], and varying the free-evolution time t_2, the population of the nth diffraction order after the second pulse can be obtained by calculating the momentum-dependent evolution operators (see Appendix A). For an initial condition $C_{2n}(k) = \delta_{n,0}$, the corresponding final population number $C_{0,\text{fin}}(k)$ is

$$C_{0,\text{fin}}(k) = (1 + e^{-i\sigma(k)}\cos\Delta\sigma(k))/2, \quad (1)$$

where $\sigma = 2\hbar k_0^2 t_2/m$, and $\Delta\sigma = 2\hbar k_0 k t_2/m$. After integrating $|C_{0,\text{fin}}|^2$ over k, the population of packet around $k = 0$ satisfies

$$P_{0\hbar k_0}(t_2) = \int_{-\infty}^{\infty} |\Phi_{\text{ini}}(k)(1 + e^{-i\sigma}\cos\Delta\sigma)|^2 dk/4. \quad (2)$$

It is well known that trapped BECs possess extremely narrow momentum widths, which is well suitable as a demonstration of our approach. For a harmonic trapped BEC, in the Thomas-Fermi approximation the momentum
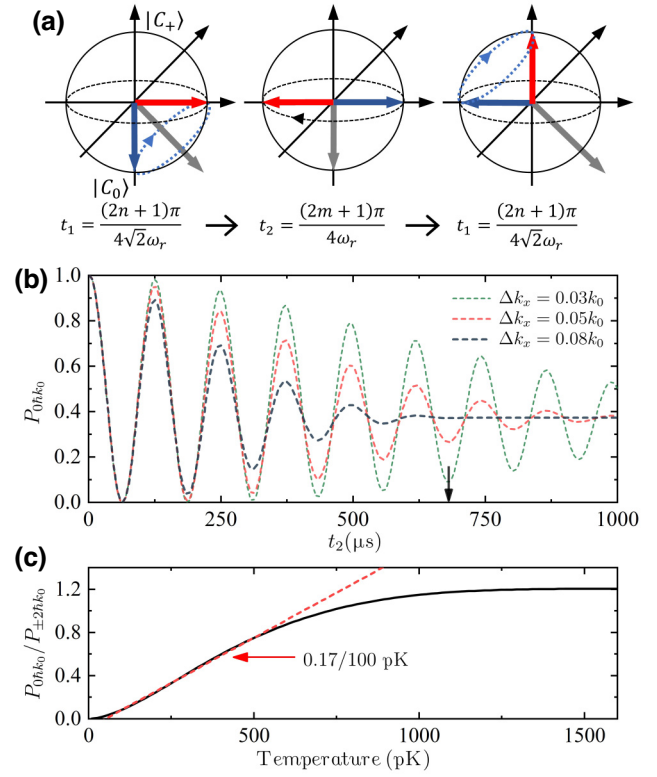

FIG. 1. (a) The Bloch-sphere interpretation of the double-pulse-splitting operation. Gray arrows denote the Rabi vectors. Blue and red arrows represent the initial and final state vectors of each individual process. n and m represent natural numbers. (b) The final population of zero-momentum term versus free-evolution duration for $\Delta k_x = 0.03k_0, 0.05k_0, 0.08k_0$, respectively. The black arrow indicates $t_2 = 5.5 \times T_{\text{osi}}$ ($T_{\text{osi}} = 123.27$ μs for the optical lattice wavelength $\lambda = 1064$ nm). (c) The relationship between population ratio and the temperature. Black solid line represents the population ratio of $0\hbar k_0$ to $\pm 2\hbar k_0$ verse temperature at $t_2 = 5.5 \times T_{\text{osi}}$. The red dashed line represents the fit about the linear region.

distribution along the x axis is given by [24,36]

$$|\Phi(k_x)|^2 = A^2 \Delta k_x^{-1} \left| \frac{J_2(\sqrt{21/8}k_x/\Delta k_x)}{(\sqrt{21/8}k_x/\Delta k_x)^2} \right|^2, \quad (3)$$

where $A^2 = N \times 315\sqrt{21/8}/64$ is the normalization coefficient, J_2 donates the Bessel function of order 2 and N is the atoms number. The momentum width $\Delta k_x = \sqrt{21/8}/R_x$, and R_x is the Thomas-Fermi radius. The corresponding equivalent temperature $T_{\text{eff}} = \Delta k_x^2 \hbar^2/k_B m$. We numerically calculate various conditions with different Δk_x, which are presented in Fig. 1(b). The population oscillation period is $T_{\text{osi}} = \pi/2\omega_r$. Due to the nonzero momentum width, after sufficiently long t_2 the contrast of the interference fringes will drop to zero, and the characteristic time is inversely proportional to Δk and k_0 [31].

Therefore, the momentum width can be determined by observing the decay rate of the contrast.

Our thermometry strategy involves selecting an appropriate t_2 based on the desired temperature range. After the double pulse, the packet will separate in space after sufficient TOF. Then, the population ratio $P_{0\hbar k_0}/P_{\pm 2\hbar k_0}$ can be conveniently counted to determine the temperature. Figure 1(c) demonstrates $P_{0\hbar k_0}/P_{\pm 2\hbar k_0}$ versus temperature for a fixed t_2, and the linear range below 500 pK is well suitable for temperature measurements. For a temperature measurement method, a useful metric is measurement accuracy. For our technique, the measured quantity is the population ratio of each momentum state, which is a macroscopic quantity that can be measured with an accuracy of 1%. However, errors in the optical lattice pulse parameters, such as amplitude, pulse length, and interval, can introduce measurement errors. Nevertheless, with the current technology, the total measurement error resulting from these factors can be easily reduced to less than 1% through optical intensity feedback control and accurate timing. Additionally, in the context of space applications, vibrations in the space station can also lead to drifts in the optical lattice during the measurement process. After implementing vibration isolation, the residual acceleration in the space station can be reduced to below 10^{-4}m/s^2 (RMS) [37]. For typical measurement durations (approximately 1 ms), the drift amplitude of the optical lattice is on the order of subnanometers, which is much smaller than the laser wavelength of the optical lattice. Therefore, we conservatively estimate that the measurement error attributed to our thermometry method is no more than 5%. For comparison, previous experiments conducted on the International Space Station [8] and the German Bremen Drop Tower [9] have measured the temperature of atomic samples using the TOF method. Their measurement accuracy, after a TOF time of several hundred milliseconds, is approximately 10%.

We would like to emphasize the measurement range of our method. Obviously a longer t_2 leads to a higher measurement accuracy. On the other hand, as Δk approaches k_0, the wave packets cannot be well separated in space after TOF, and the two-level approximation is no longer valid. Therefore, the upper limit is constrained by the single-photon recoil momentum of the optical lattice. To expand the measurement range and reduce pulse durations t_1 and free evolution time t_2, an optical lattice with shorter laser wavelength would be advantageous [31].

III. EXPERIMENTAL IMPLEMENTATION

We experimentally measured the 1D MW of a BEC *in situ* by double-pulse splitting, and the experimental setup and protocol are illustrated in Figs. 2(a) and 2(b). We prepared the initial 5×10^4 ^{87}Rb BEC in a 1064-nm crossed optical dipole trap, with the trap frequency of $\nu =$
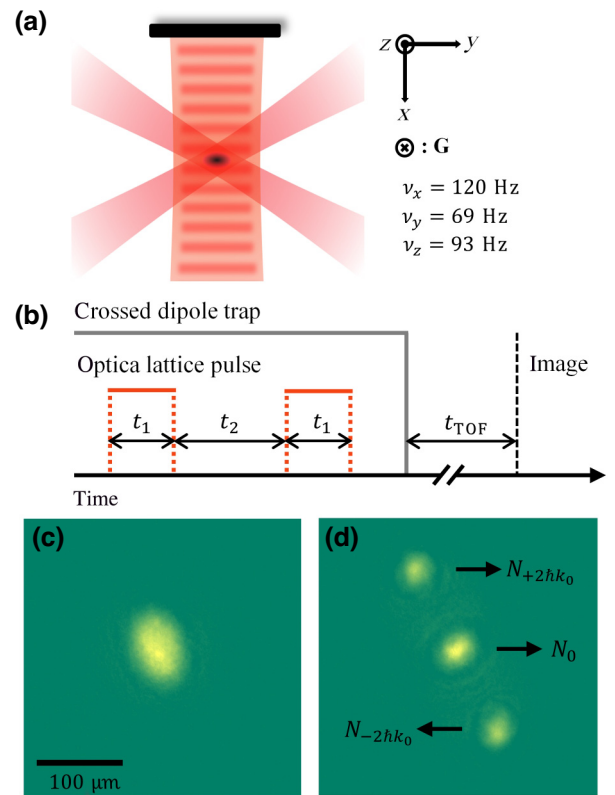

FIG. 2. (a) Experimental setup. The BEC is initially trapped in a crossed dipole trap consisting of two 1064-nm laser beams intersecting at 60°. Another 1064-nm beam (independent laser) incidents horizontally along the x axis and be reflected to form the one-dimensional optical lattice. (b) Experimental protocol. The duration of a single optical lattice pulse is fixed at 43.59 µs. (c) Absorption image of the initial BEC. (d) Absorption image of the cloud after double-pulse splitting with $t_2 = 90$ µs as an example.

$(120, 69, 93)$ Hz along the x, y, and z directions. The condensate fraction was approximately 60%, and the atoms were approximately uniformly populated in the three Zeeman states of the ground manifold $|5^2S_{1/2}, F = 1\rangle$. In the Thomas-Fermi limit, the momentum width of the initial BEC can be estimated as [38] $\Delta k = (0.07, 0.04, 0.054) k_0$. After obtaining the initial BEC through forced evaporative cooling, we applied two 1064-nm laser standing-wave pulses to the BEC while maintaining the optical trap. Subsequently, we released the atoms and performed conventional absorption imaging after 25-ms TOF. Figures 2(c) and 2(d) demonstrate the splitting result, and then we counted the populations of different diffraction orders. The noncondensate atoms will disturb the statistics of the population. Indeed, thermal atoms also respond to the double pulse, but it will be quite different compared to the case of BEC. For relatively high temperatures ($T_{\text{thermal}} \sim 100$ nK), the corresponding coherence length is very short, leading to rapid dephasing. In fact, the population of different momentum states of thermal atoms hardly changes with
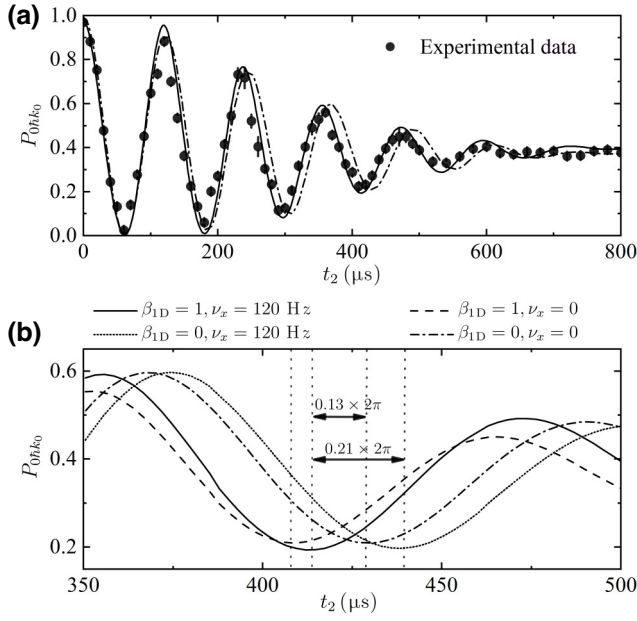
FIG. 3. Temporal evolution of the zero-momentum term population. (a) The experimental results are represented by black circles, and the error bars indicate the standard deviation of five runs. The numerical results of the GP equation are shown by the different lines. The simulation parameters used are $\Delta k_x = 0.075k_0$, $\kappa_{1D} = 0.02$, and $s = 3.05$. (b) Numerical simulation results under different conditions around $t_2 = 3.5 \times T_{\text{osi}}$ [the curve with $\beta_{1D} = 0, \nu_x = 0$ is calculated from Eq. (2)]. Those vertical dotted lines mark the bottoms of this oscillation period, respectively, and the horizontal arrows indicate the corresponding phase differences.

the increase in Ramsey free-evolution time. Additionally, after releasing the atoms and undergoing a 25-ms TOF, the optical depth of thermal atoms is very small, thus having little impact on the statistical measurement of the population ratio of different diffraction orders of BEC.

Figure 3(a) illustrates the experimental results of the final zero-momentum population versus t_2, demonstrating a clear oscillation decay. Our theory accurately captures this characteristic behavior, yet we noted that the oscillation period T_{osi} is slightly shorter than predicted, which becomes more evident after sufficiently long free-evolution times. By using Δk_x and the optical lattice laser wavelength λ as fitting parameters and applying Eq. (2), we obtained $\Delta k_x = 0.067k_0$ and $\lambda = 1040$ nm. This mismatch is not particularly surprising, actually, in our simplified theory we neglected the trap potential and interatomic interactions, while neither can be ignored in our experiments.

IV. NUMERICAL SIMULATION AND PHASE-SPACE EVOLUTION

To interpret our experimental results, we employed numerical calculations of the 1D *Gross-Pitaevskii* equation

[39] (GP equation) to simulate the entire experimental process. The dimensionless GP equation can be expressed as

$$i\dot{\psi}_\alpha(x,t) = \left(-\frac{1}{2}\frac{d}{dx^2} + \frac{x^2}{2} + \Omega(t)\cos 2k_0 x \right.$$
$$\left. + \beta_{1D}\kappa_{1D}U_0 \sum_{\alpha'} |\psi_{\alpha'}|^2 \right) \psi_\alpha(x,t), \quad (4)$$

where ψ_α donate wave functions of different spin components ($\alpha = 0, \pm 1$), $U_0 = 4\pi a_s N/a_0$, a_s is the two-body s-wave scattering length, $a_0 = \sqrt{\hbar/2\pi m \nu_x}$, κ_{1D} is a fitting parameter that represents reduced-dimensionality factor [40], and β_{1D} is equal to 0 or 1 that controls whether the nonlinear term exists. We have verified the rationality of κ_{1D} in Appendix B. The modulus of the Fourier transformation of $\Phi(k_x)$ was adopted as the initial macroscopic wave function, and Δk_x was taken as a fitting parameter. To account for calibration errors in the optical lattice depth, we also used $\Omega = s\omega_r$ as a fitting parameter during the pulse. Considering that we used the $F = 1$ spinor BEC in the experiment, we adopted the multicomponent GP equations. If the initial states of the wave functions of the three spin components are identical, the corresponding evolution can be reduced to the single-component case.

The simulation result is also displayed in Fig. 3(a), which is in good agreement with the experimental results. The fitting parameter $\Delta k_x = 0.075k_0$ also coincides with $0.07k_0$ obtained in the Thomas-Fermi approximation. We demonstrate the simulation results for several other cases in Fig. 3(c), and it is evident that the interatomic interactions slightly accelerate the evolution of the population, while the trap potential has the opposite effect. The actual evolution is determined by the competition between these two effects.

Despite the perfect description of experimental results by the GP equations, the underlying physical meaning remains obscure. We introduce the Wigner function to provide a more intuitive interpretation of the double-pulse splitting process. The Wigner function describes a quasiprobability distribution in the phase space, with values that can be both positive and negative [41,42]. We can use the momentum space wave function to construct the Wigner function:

$$W(x, k_x; t) = \int_{-\infty}^{\infty} dp\, e^{ipx} \Phi(-k_x - p/2, t)\Phi^*(-k_x + p/2, t).$$
$$(5)$$

Let us first consider the scenario that excludes external trap and mean-field interaction. In Figs. 4(a)–4(c), we present the corresponding Wigner functions at various time points. Following the first pulse, the wave function becomes a superposition of three momentum states. In

addition to the three regions with central momentum $0\hbar k_0$ and $\pm 2\hbar k_0$, Fig. 4(a) reveals the presence of interference terms between $2n\hbar k_0$ and $2m\hbar k_0$, which are located at $(n+m)\hbar k_0$, appearing as fringes in phase space with a spatial frequency of $|2(n-m)k_0|$ [31].

During the free evolution, the time evolution of the Wigner function follows the classical equation of motion [41]. Therefore, as t_2 increases, wave packets with different momentum tend to separate in space, and the fringes in the interference region will tilt more and more. This tilt of fringes indicates that, due to the finite momentum width, the phases of different momentum components are no longer the same after free evolution. It is well known that BEC as a macroscopic coherent state possessing the *off-diagonal long-ranged order* (ODLRO), which implies that the coherent length approaches the macroscopic size of the condensate [43,44]. Once these three wave packets are completely separated, coherence between them will be concealed. When the second pulse is applied, the population of the central zero momentum is merely the sum of the zero momentums originating from the independent splitting of the three parts, as depicted in Fig. 4(c). The hiding of coherence means that the contrast of the interference fringe drops to zero and $P_{0\hbar k_0}$ will no longer change. The momentum distribution after the double pulses is shown in Fig. 4(d) as a sample.

Next, we add the external trap and mean-field interaction separately to observe the changes. Due to the relatively short pulse duration, the corresponding phase-space distribution undergoes only slight changes in comparison to Fig. 4(a) during the first pulse, thus we did not show them. However, after sufficiently long free-evolution times, the phase-space distributions under different conditions exhibits significant divergence. For the case with only external trap in Fig. 4(e), the evolution of the Wigner function is just a clockwise rotation in phase-space corresponding to simple harmonic oscillation in the trap. On the other hand, the nonlinear term causes wave packets in different regions to broaden in both the spatial and momentum domains, as shown in Fig. 4(f). This is essentially a rapid explosion of the condensate caused by the repulsive mean-field interaction. When both the external trap and nonlinear term are considered, the two effects partially counteract each other, as illustrated in Fig. 4(g).

Furthermore, we display the momentum distribution around $+2\hbar k_0$ in Fig. 4(h) under various conditions. On our experimental timescale, except for the acceleration effect, either the external trap or the nonlinear term broadens the momentum distribution. However, the synergistic cooperation of these two effects significantly reduces the degree of broadening. As an estimate, we utilize Gaussian
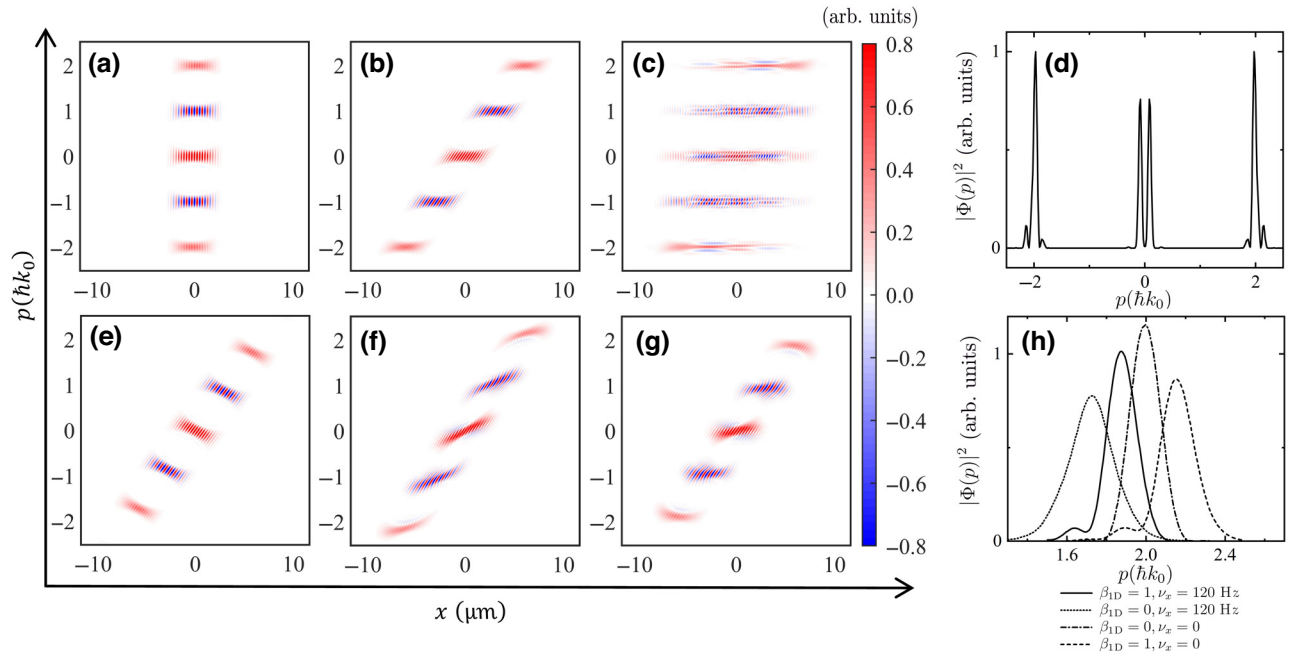

FIG. 4.   (a) The phase-space distribution just after the first pulse. (b) The phase-space distribution after free evolution with $t_2 = 5.5 \times T_{\mathrm{osi}}$, and the three parts with central momentum $0\hbar k_0$ and $\pm 2\hbar k_0$ are basically separated in space. (c) The phase-space distribution just after the second pulse. (a)–(c) are based on completely free evolution, i.e., in the absence of the external trap and nonlinear term. (d) The momentum distribution after the pulse sequence. (e)–(g) The phase-space distributions after free evolution $t_2 = 5.5 \times T_{\mathrm{osi}}$ comprise of only the external trap, only the nonlinear term, and both, respectively. (h) The momentum distribution of the $+2\hbar k_0$ diffraction order under different conditions.

fits to confirm that the change in momentum width is no more than 5%.

V. MECHANISM OF ACCELERATED PHASE ACCUMULATION

In addition to broadening the distribution, there is still a net momentum offset during free evolution, which can be evaluated using the average momentum $\langle k \rangle_{+2}$ of the first diffraction order. Figure 5(a) displays the evolution of $\langle k \rangle_{+2}$ with respect to t_2. Our simulations indicate that the acceleration caused by the repulsive mean-field interaction saturates after 400 μs. With the further addition of external trap, the evolution of $\langle k \rangle_{+2}$ is essentially a straightforward superposition of these two effects, resulting in an initial rise followed by a fall. We can evaluate the accumulated phase by integrating the square of the average momentum

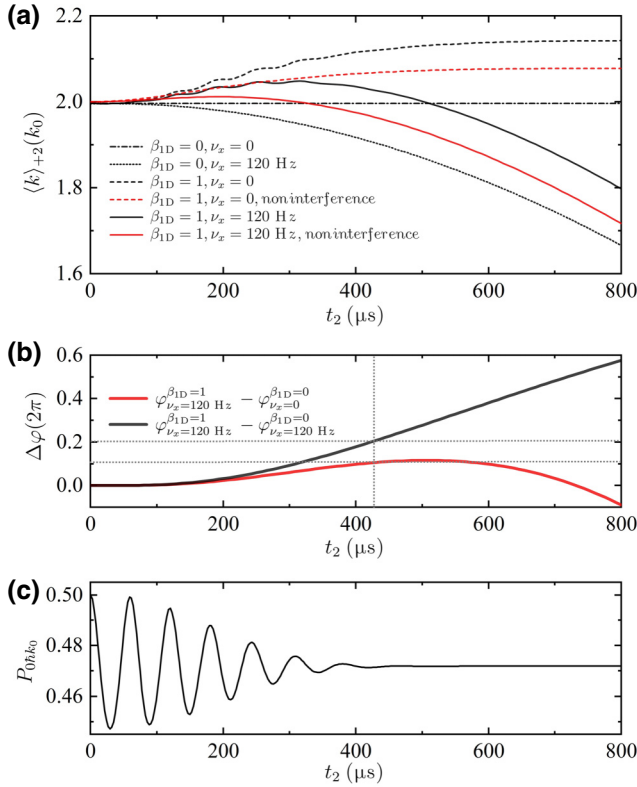$$\varphi = \int_0^{t_2} dt 2\hbar t \langle k \rangle_{+2}^2 / m. \qquad (6)$$

(a)

(b)

(c)

FIG. 5. (a) The evolution of the average momentum of the $+2\hbar k_0$ diffraction order with respect to t_2. The noninterference cases indicate the initial entanglement state. (b) The phase difference accumulated due to distinct average momentums. The vertical dashed line at $t_2 = 425$ μs indicates the corresponding phase differences of $0.11 \times 2\pi$ and $0.20 \times 2\pi$, respectively. (c) The population evolution of the central zero-momentum state during the free evolution caused by the nonlinear term and spatial density modulation.

Figure 5(b) shows the accumulated phase difference versus t_2, with the corresponding values of $\Delta\varphi = 0.11 \times 2\pi$ and $0.20 \times 2\pi$ at $t_2 = 425\mu s$ for the two curves, which are semiquantitatively consistent with $\Delta\varphi = 0.13 \times 2\pi$ and $0.21 \times 2\pi$ as evaluated in Fig. 3(b), respectively.

The additional acceleration effect caused by the nonlinear term is, in fact, a bit more subtle. We observe an intricate oscillatory growth behavior before $\langle k \rangle_{+2}$ reaches saturation, with the period of oscillation consistent with the time it takes for an atom with momentum $2\hbar k_0$ to travel a distance of $\lambda/2$. Actually, the interference between different momentum components implies a spatially periodic modulation of the wave function with a period of $\lambda/2$. Under the local density approximation, the effective potential felt by atoms is just a superposition of the local chemical potential and external trap potential, which can be regarded as a "matter wave lattice." This is reminiscent of the self-phase modulation of light waves propagating in a Kerr medium. Therefore, we anticipate additional population transformation during the free evolution due to the mean-field interaction, which is also confirmed by our simulations, as shown in Fig. 5(c). After 400 μs, the population ceases to evolve due to the separation of different momentum states, such that the spatial modulation of density is no longer well periodicity. Notably, the trend of the population oscillation coincides with the oscillatory growth of the average momentum in Fig. 5(a), indicating that the acceleration effect actually originates from the spatial density modulation.

We present a specific scenario to substantiate this viewpoint. Specifically, we consider the three spin components that are initially spatially overlapped and entangled with the external states.

$$|\phi\rangle_{\text{ini}} = \frac{1}{\sqrt{2}} |0\rangle_{m_F} \otimes |0\rangle_k + \frac{1}{2} |1\rangle_{m_F} \otimes |2k_0\rangle_k$$
$$+ \frac{1}{2} |-1\rangle_{m_F} \otimes |-2k_0\rangle_k. \qquad (7)$$

One distinction is that, owing to the orthogonality of internal states, there is no longer interference among the various momentum states. We calculate the subsequent free evolution based on the three-components GP equations, and the corresponding results are also shown in Fig. 5(a). It is evident that the acceleration effect is significantly curtailed when compared to the coherent case (with the same atomic number). Upon further addition of the external trap, the initial acceleration is almost entirely suppressed. This can be understood as the repulsive interaction and external trap potential canceling each other out, leading to the atoms feeling a flattened effective potential.

Our simulation and analysis results indicate that the effect of interatomic interactions requires care. Intriguingly, the presence of the nonlinear term accelerates the entire double-pulse-splitting process, or rather accelerates

the bit flip. On the other hand, compared to our demonstration experiment, in conventional deep-cooling procedure, the adiabatic expansion method will reduce the trap frequency to an extremely low range (approximately 1 Hz), while the DKC method allows the BEC to expand freely for a moment before collimation, both extremely reduce the interaction energy of the BEC (2 orders of magnitude compared to our case) [45], rendering the nonlinear term negligible.

VI. CONCLUSION

In conclusion, we employed a Bragg-splitting-type atomic interference strategy to measure the momentum width of a BEC *in situ*. By utilizing suitable double-pulse sequences, we split the atomic samples and subsequently determine the coherence length to calibrate the temperature. Remarkably, we observed intriguing dynamical effect induced by the mean-field interaction and spatial density modulation of the BEC during the interference process, and analyzed this effect in detail. Our quantum thermometry is particularly suitable for temperature calibration of ultracold Bose atomic samples at the pK level.

ACKNOWLEDGMENTS

APPENDIX A: DERIVATION OF EVOLUTIONARY OPERATORS

Firstly, we consider the evolution operator during the implement of a single pulse. In the coupled bases ($|C_0(k)\rangle$, $|C_+(k)\rangle$, $|C_-(k)\rangle$), for the initial conditions $C_{2n}(k) = \delta_{n,0}$, a $\pi/2$ pulse translates $|C_0(k)\rangle$ to $(|C_0(k)\rangle + |C_+(k)\rangle)/\sqrt{2}$, which is equivalent to a Hadamard gate, and the corresponding evolution matrix is:

$$U_c(t_1) = \begin{bmatrix} 1/\sqrt{2} & 1/\sqrt{2} & 0 \\ 1/\sqrt{2} & -1/\sqrt{2} & 0 \\ 0 & 0 & 1 \end{bmatrix}. \tag{A1}$$

Next, we consider the free evolution in momentum bases ($|C_0(k)\rangle$, $|C_{+2k_0}(k)\rangle$, $|C_{-2k_0}(k)\rangle$). $|C_{+2k_0}(k)\rangle$ has higher energy than $|C_0(k)\rangle$ by

$$\Delta E_{+2k_0} = \hbar^2[(2k_0 + k)^2 - k^2]/2m. \tag{A2}$$

Such that after the free evolution of t_2, the accumulated phase difference between $|C_{+2k_0}(k)\rangle$ and $|C_0(k)\rangle$ is

$$\sigma_{+2k_0}(k) = \Delta E_{+2k_0} t_2/\hbar = 2\hbar k_0(k_0 + k)t_2/m. \tag{A3}$$

We can separate σ_{+2k_0} as $\sigma = 2\hbar k_0^2 t_2/m$ describing the phase delay corresponding the central momentum difference during the free evolution, and $\Delta\sigma = 2\hbar k_0 k t_2/m$ describing the contribution from nonzero k, such that $\sigma_{+2k_0} = \sigma + \Delta\sigma$. Similarly, the phase difference between $|C_{-2k_0}(k)\rangle$ and $|C_0(k)\rangle$ could be expressed as $\sigma_{-2k_0} = \sigma - \Delta\sigma$. The free evolution corresponds to a phase gate, and up to a global phase factor, the corresponding evolution matrix is

$$U(t_2) = \begin{bmatrix} 1 & 0 & 0 \\ 0 & e^{-i\sigma_{+2k_0}(k)} & 0 \\ 0 & 0 & e^{-i\sigma_{-2k_0}(k)} \end{bmatrix}$$

$$= \begin{bmatrix} 1 & 0 & 0 \\ 0 & e^{-i(\sigma+\Delta\sigma(k))} & 0 \\ 0 & 0 & e^{-i(\sigma-\Delta\sigma(k))} \end{bmatrix}. \tag{A4}$$

The unitary operator to translate the momentum bases to the coupled bases is

$$S = S^\dagger = S^{-1} = \begin{bmatrix} 1 & 0 & 0 \\ 0 & 1/\sqrt{2} & 1/\sqrt{2} \\ 0 & 1/\sqrt{2} & -1/\sqrt{2} \end{bmatrix}. \tag{A5}$$

Therefore, the total evolution operator in the coupled bases is

$$U_c(2t_1 + t_2) = U_c(t_1)S^\dagger U(t_2)SU_c(t_1) = \begin{bmatrix} \dfrac{1 + e^{-i\sigma}\cos\Delta\sigma}{2} & \dfrac{1 - e^{-i\sigma}\cos\Delta\sigma}{2} & \dfrac{-ie^{-i\sigma}\sin\Delta\sigma}{\sqrt{2}} \\ \dfrac{1 - e^{-i\sigma}\cos\Delta\sigma}{2} & \dfrac{1 + e^{-i\sigma}\cos\Delta\sigma}{2} & \dfrac{ie^{-i\sigma}\sin\Delta\sigma}{\sqrt{2}} \\ \dfrac{-ie^{-i\sigma}\sin\Delta\sigma}{\sqrt{2}} & \dfrac{ie^{-i\sigma}\sin\Delta\sigma}{\sqrt{2}} & e^{-i\sigma}\cos\Delta\sigma \end{bmatrix}. \tag{A6}$$

Translate to the momentum bases:

$$U(2t_1 + t_2) = SU_c(2t_1 + t_2)S^\dagger. \qquad (A7)$$

Therefore, the corresponding final state in the momentum bases for an initial condition $C_{2n}(k) = \delta_{n,0}$ is

$$\begin{bmatrix} C_0 \\ C_{+2k_0} \\ C_{-2k_0} \end{bmatrix}_{\text{fin}}$$

$$= U(2t_1 + t_2) \begin{bmatrix} 1 \\ 0 \\ 0 \end{bmatrix}$$

$$= \begin{bmatrix} (1 + e^{-i\sigma}\cos\Delta\sigma)/2 \\ (1 - e^{-i\sigma}\cos\Delta\sigma - ie^{-i\sigma}\sqrt{2}\sin\Delta\sigma)/2\sqrt{2} \\ (1 - e^{-i\sigma}\cos\Delta\sigma + ie^{-i\sigma}\sqrt{2}\sin\Delta\sigma)/2\sqrt{2} \end{bmatrix}. \qquad (A8)$$

In the main text, the applied pulse intensity and duration are derived from the truncated RNEs [34], however, we would like to emphasize that truncating the RNEs to the second order will slightly reduce the fidelity of the entire operation due to the imperfect pulse strength and duration. In our previous work [31], we have evaluated this issue meticulously by using the more precise Bloch band theory [46]. Despite the slight disparities between these two approaches, without affecting the main results, we still use the two-level approximation for simplicity, and the principal conclusions of this paper remain unaffected.

APPENDIX B: NUMERICAL CALCULATION OF THE 1D GP EQUATION

We adopt *alternate direction implicit time-splitting pseudospectral (ADI TSSP)* schemes to numerically calculate the 1D *Gross-Pitaevskii* equation [39],

$$i\hbar\dot{\psi}_\alpha(x,t) = (-\frac{\hbar^2}{2m}\frac{d}{dx^2} + \frac{m\omega^2 x^2}{2} + \Omega(t)\cos 2k_0 x$$

$$+ \beta_{1D}\kappa_{1D}g\sum_{\alpha'}|\psi_{\alpha'}|^2)\psi_\alpha(x,t), \qquad (B1)$$

where $g = 4\pi\hbar^2 a_s/m$. The dimensionless equation is derived by introducing the following changes of variables:

$$t \rightarrow t/\omega_x, x \rightarrow xa_0, a_0 = \sqrt{\hbar/2\pi m\nu_x},$$

$$\psi_\alpha \rightarrow \psi_\alpha/\sqrt{a_0}, \Omega \rightarrow \Omega\omega_x, g = 2\pi a_0^3\hbar\nu_x U_0/N. \qquad (B2)$$

Due to the nearly identical singlet and triplet scattering lengths for $F = 1$ ^{87}Rb atoms, we have neglected the two-atom spin-exchange reactions [47,48]. For the case without trap potential and nonlinear term, the numerical calculation result is basically identical to the evolution operator
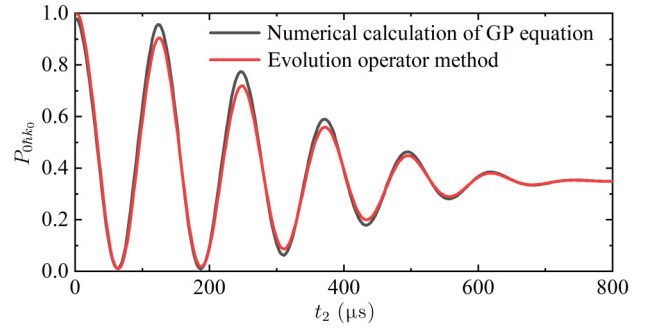

FIG. 6. Comparison between the numerical calculation result of GP equation and evolutionary operator method.

method, as shown in Fig. 6. Next we check the plausibility of the free parameter κ_{1D} used in our simulation. In the Thomas-Fermi approximation, the condensate wave function is

$$\psi(x,y,z) = \sqrt{n_0\left[1 - \sum_{i=x,y,z}\left(\frac{r_i}{R_i}\right)^2\right]}. \qquad (B3)$$

The reduced-dimensionality factor κ_{1D} can be obtained by [40]

$$\kappa_{1D} = \iint |\psi(y,z)|^4 dydz. \qquad (B4)$$

The application of Eq. (B4) requires the wave function to be variable separable over the reduced dimension, however, Eq. (B3) does not satisfy this assumption. Nevertheless, we can utilize a trial function to estimate κ_{1D}.

$$\psi_{\text{tri}}(x,y,z) = \frac{N^{1/2}}{\pi^{3/4}(b_x b_y b_z)^{1/2}}e^{-x^2/2b_x^2}e^{-y^2/2b_y^2}e^{-z^2/2b_z^2}, \qquad (B5)$$

where the lengths b_i are variational parameters. After minimizing the energy by calculus of variations [38], we can get

$$b_i = (2/\pi)^{1/10}(Na_s/\bar{a})^{1/5}\bar{\omega}\bar{a}/\omega_i, \qquad (B6)$$

where $\bar{\omega} = \sqrt[3]{\omega_x\omega_y\omega_z}$ and $\bar{a} = (\hbar/m\bar{\omega})^{1/2}$, thus $\kappa_{1D} \sim 1/2\pi b_y b_z$. After the nondimensionalization (replace b_i with b_i/a_0), this value is about 0.014, such that it verifies our fitting parameter κ_{1D} is within reasonable range.

[1] A. J. Leggett, Bose-Einstein condensation in the alkali gases: Some fundamental concepts, Rev. Mod. Phys. **73**, 307 (2001).

[2] X. Chen and B. Fan, The emergence of picokelvin physics, Rep. Prog. Phys. **83**, 076401 (2020).

[3] A. Bassi, K. Lochan, S. Satin, T. P. Singh, and H. Ulbricht, Models of wave-function collapse, underlying theories, and experimental tests, Rev. Mod. Phys. **85**, 471 (2013).

[4] S. Nimmrichter and K. Hornberger, Macroscopicity of Mechanical Quantum Superposition States, Phys. Rev. Lett. **110**, 160403 (2013).

[5] A. E. Leanhardt, T. A. Pasquini, M. Saba, A. Schirotzek, Y. Shin, D. Kielpinski, D. E. Pritchard, and W. Ketterle, Cooling Bose-Einstein condensates below 500 picokelvin, Science **301**, 1513 (2003).

[6] H. Ammann and N. Christensen, Delta Kick Cooling: A New Method for Cooling Atoms, Phys. Rev. Lett. **78**, 2088 (1997).

[7] T. Kovachy, J. M. Hogan, A. Sugarbaker, S. M. Dickerson, C. A. Donnelly, C. Overstreet, and M. A. Kasevich, Matter Wave Lensing to Picokelvin Temperatures, Phys. Rev. Lett. **114**, 143004 (2015).

[8] N. Gaaloul, M. Meister, R. Corgier, A. Pichery, P. Boegel, W. Herr, H. Ahlers, E. Charron, J. R. Williams, R. J. Thompson, W. P. Schleich, E. M. Rasel, and N. P. Bigelow, A space-based quantum gas laboratory at picokelvin energy scales, Nat. Commun. **13**, 7889 (2022).

[9] C. Deppner, W. Herr, M. Cornelius, P. Stromberger, T. Sternke, C. Grzeschik, A. Grote, J. Rudolph, S. Herrmann, M. Krutzik, A. Wenzlawski, R. Corgier, E. Charron, D. Guéry-Odelin, N. Gaaloul, C. Lämmerzahl, A. Peters, P. Windpassinger, and E. M. Rasel, Collective-Mode Enhanced Matter-Wave Optics, Phys. Rev. Lett. **127**, 100401 (2021).

[10] M. Greiner, O. Mandel, T. Esslinger, T. W. Hänsch, and I. Bloch, Quantum phase transition from a superfluid to a Mott insulator in a gas of ultracold atoms, Nature **415**, 39 (2002).

[11] L. Niu, S. Jin, X. Chen, X. Li, and X. Zhou, Observation of a Dynamical Sliding Phase Superfluid with P-Band Bosons, Phys. Rev. Lett. **121**, 265301 (2018).

[12] I. M. Georgescu, S. Ashhab, and F. Nori, Quantum simulation, Rev. Mod. Phys. **86**, 153 (2014).

[13] S. Banik, M. G. Galan, H. Sosa-Martinez, M. Anderson, S. Eckel, I. B. Spielman, and G. K. Campbell, Accurate Determination of Hubble Attenuation and Amplification in Expanding and Contracting Cold-Atom Universes, Phys. Rev. Lett. **128**, 090401 (2022).

[14] J. Steinhauer, Observation of quantum Hawking radiation and its entanglement in an analogue black hole, Nat. Phys. **12**, 959 (2016).

[15] H. Ahlers, H. Müntinga, A. Wenzlawski, M. Krutzik, G. Tackmann, S. Abend, N. Gaaloul, E. Giese, A. Roura, R. Kuhl, C. Lämmerzahl, A. Peters, P. Windpassinger, K. Sengstock, W. P. Schleich, W. Ertmer, and E. M. Rasel, Double Bragg Interferometry, Phys. Rev. Lett. **116**, 173601 (2016).

[16] S. Abend, M. Gebbe, M. Gersemann, H. Ahlers, H. Müntinga, E. Giese, N. Gaaloul, C. Schubert, C. Lämmerzahl, W. Ertmer, W. P. Schleich, and E. M. Rasel, Atom-Chip Fountain Gravimeter, Phys. Rev. Lett. **117**, 203003 (2016).

[17] S.-w. Chiow and N. Yu, Compact atom interferometer using single laser, Appl. Phys. B **124**, 96 (2018).

[18] G. Rosi, F. Sorrentino, L. Cacciapuoti, M. Prevedelli, and G. M. Tino, Precision measurement of the Newtonian gravitational constant using cold atoms, Nature **510**, 518 (2014).

[19] J. M. Hogan and M. A. Kasevich, Atom-interferometric gravitational-wave detection using heterodyne laser links, Phys. Rev. A **94**, 033632 (2016).

[20] S. Kolkowitz, I. Pikovski, N. Langellier, M. D. Lukin, R. L. Walsworth, and J. Ye, Gravitational wave detection with optical lattice atomic clocks, Phys. Rev., D **94**, 124043 (2016).

[21] J. Williams, S.-w. Chiow, N. Yu, and H. Müller, Quantum test of the equivalence principle and space-time aboard the International Space Station, New J. Phys. **18**, 025018 (2016).

[22] P. D. Lett, R. N. Watts, C. I. Westbrook, W. D. Phillips, P. L. Gould, and H. J. Metcalf, Observation of Atoms Laser Cooled below the Doppler Limit, Phys. Rev. Lett. **61**, 169 (1988).

[23] M. Kasevich, D. S. Weiss, E. Riis, K. Moler, S. Kasapi, and S. Chu, Atomic Velocity Selection using Stimulated Raman Transitions, Phys. Rev. Lett. **66**, 2297 (1991).

[24] J. Stenger, S. Inouye, A. P. Chikkatur, D. M. Stamper-Kurn, D. E. Pritchard, and W. Ketterle, Bragg Spectroscopy of a Bose-Einstein Condensate, Phys. Rev. Lett. **82**, 4569 (1999).

[25] B. Deh, C. Marzok, S. Slama, C. Zimmermann, and P. W. Courteille, Bragg spectroscopy and Ramsey interferometry with an ultracold Fermi gas, Appl. Phys. B **97**, 387 (2009).

[26] J. R. Kellogg, N. Yu, J. M. Kohel, R. J. Thompson, D. C. Aveline, and L. Maleki, Longitudinal coherence in cold atom interferometry, J. Mod. Opt. **54**, 2533 (2007).

[27] S. S. Szigeti, J. E. Debs, J. J. Hope, N. P. Robins, and J. D. Close, Why momentum width matters for atom interferometry with Bragg pulses, New J. Phys. **14**, 023009 (2012).

[28] B. Saubaméa, T. W. Hijmans, S. Kulin, E. Rasel, E. Peik, M. Leduc, and C. Cohen-Tannoudji, Direct Measurement of The Spatial Correlation Function of Ultracold Atoms, Phys. Rev. Lett. **79**, 3146 (1997).

[29] P. D. Featonby, G. S. Summy, C. L. Webb, R. M. Godun, M. K. Oberthaler, A. C. Wilson, C. J. Foot, and K. Burnett, Separated-Path Ramsey Atom Interferometer, Phys. Rev. Lett. **81**, 495 (1998).

[30] M. Carey, J. Saywell, D. Elcock, M. Belal, and T. Freegarde, Velocimetry of cold atoms by matter-wave interferometry, Phys. Rev. A **99**, 023631 (2019).

[31] S. Zhou, C. Chen, B. Xu, A. Liang, Y. Wang, and B. Wang, Characterizing ultra-narrow momentum of atoms by standing-wave light-pulse sequences, J. Opt. Soc. Am. B **39**, 3012 (2022).

[32] C. Adams, M. Sigel, and J. Mlynek, Atom optics, Phys. Rep. **240**, 143 (1994).

[33] Y.-J. Wang, D. Z. Anderson, V. M. Bright, E. A. Cornell, Q. Diot, T. Kishimoto, M. Prentiss, R. A. Saravanan, S. R. Segal, and S. Wu, Atom Michelson Interferometer on a Chip Using a Bose-Einstein Condensate, Phys. Rev. Lett. **94**, 090405 (2005).

[34] S. Wu, Y.-J. Wang, Q. Diot, and M. Prentiss, Splitting matter waves using an optimized standing-wave light-pulse sequence, Phys. Rev. A **71**, 043602 (2005).

[35] C. Bordé, Atomic interferometry with internal state labelling, Phys. Lett. A **140**, 10 (1989).

[36] G. Baym and C. J. Pethick, Ground-State Properties of Magnetically Trapped Bose-Condensed Rubidium Gas, Phys. Rev. Lett. **76**, 6 (1996).

[37] W. Dong, W. Duan, W. Liu, and Y. Zhang, Microgravity disturbance analysis on Chinese space laboratory, Npj Microgravity **5**, 18 (2019).

[38] C. Pethick and H. Smith, *Bose-Einstein Condensation in Dilute Gases* (Cambridge University Press, Cambridge ; New York, 2008), 2nd ed.

[39] X. Antoine and R. Duboscq, GPELab, a Matlab toolbox to solve Gross–Pitaevskii equations II: Dynamics and stochastic simulations, Comput. Phys. Commun. **193**, 95 (2015).

[40] C. Besse and J.-C. Garreau, eds. *Nonlinear Optical and Atomic Systems: At the Interface of Physics and Mathematics*, Lecture Notes in Mathematics, Vol. 2146 (Springer International Publishing, Cham, 2015).

[41] C.-Y. Wong, Explicit solution of the time evolution of the Wigner function, J. Opt., B: Quantum Semiclass. Opt. **5**, S420 (2003).

[42] S. Liu, D. Han, N. Wang, Y. Xiang, F. Sun, M. Wang, Z. Qin, Q. Gong, X. Su, and Q. He, Experimental Demonstration of Remotely Creating Wigner Negativity via Quantum Steering, Phys. Rev. Lett. **128**, 200401 (2022).

[43] M. R. Andrews, C. G. Townsend, H.-J. Miesner, D. S. Durfee, D. M. Kurn, and W. Ketterle, Observation of interference between two Bose condensates, Science **275**, 637 (1997).

[44] A. J. Moilanen, K. S. Daskalakis, J. M. Taskinen, and P. Törmä, Spatial and Temporal Coherence in Strongly Coupled Plasmonic Bose-Einstein Condensates, Phys. Rev. Lett. **127**, 255301 (2021).

[45] T. Luan, Y. Li, X. Zhang, and X. Chen, Realization of two-stage crossed beam cooling and the comparison with Delta-kick cooling in experiment, Rev. Sci. Instrum. **89**, 123110 (2018).

[46] O. Morsch and M. Oberthaler, Dynamics of Bose-Einstein condensates in optical lattices, Rev. Mod. Phys. **78**, 179 (2006).

[47] S. Haze, J. P. D'Incao, D. Dorer, M. Deiß, E. Tiemann, P. S. Julienne, and J. H. Denschlag, Spin-Conservation Propensity Rule for Three-Body Recombination of Ultracold Rb Atoms, Phys. Rev. Lett. **128**, 133401 (2022).

[48] D. M. Stamper-Kurn and M. Ueda, Spinor Bose gases: Symmetries, magnetism, and quantum dynamics, Rev. Mod. Phys. **85**, 1191 (2013).